GEOCHEMISTRY

Elemental constraints on the amount of recycled crust in the generation of mid-oceanic ridge basalts (MORBs)

Shuying Yang[1], Munir Humayun[1]*, Vincent J. M. Salters[1]

Mid-oceanic ridge basalts (MORBs) are depleted in incompatible elements, but ridge segments far from mantle plumes frequently erupt chemically enriched MORBs (E-MORBs). Two major explanations of E-MORBs are that these basalts are generated by the melting of entrained recycled crust (pyroxenite) beneath ridges or by the melting of refertilized peridotites. These two hypotheses can be discriminated with compatible element abundances from Sc to Ge, here termed the ScGe elements. Here, we demonstrate that E-MORBs have systematically lower Ge/Si and Sc contents and slightly higher Fe/Mn and Nb/Ta ratios than depleted MORBs (D-MORBs) due to the mixing of low-degree pyroxenite melts. The Ge/Si ratio is a new tracer that effectively discriminates between melts derived from peridotite sources and melts derived from mixed pyroxenite-peridotite sources. These new data are used to estimate the distribution of pyroxenite in the mantle sources of global MORB segments.

INTRODUCTION

Mid-oceanic ridge basalts (MORBs) represent Earth's upper mantle sampled by the globe-encircling system of ridges that form the basement of the world's oceans. Low-degree partial melts from Earth's mantle preferentially extract elements that are highly incompatible in the lattices of mantle minerals, leaving behind a residue that is depleted in highly incompatible elements, the depleted MORB mantle (DMM). Subsequent melting of DMM produces MORBs (1, 2). On the basis of the abundances of highly incompatible elements, MORBs are grouped as depleted (D-MORBs), normal (N-MORBs), or enriched (E-MORBs), where N-MORBs have lower abundances of the most incompatible elements than primitive upper mantle (3). E-MORBs were first noted near mantle plumes so that enrichment of highly incompatible elements was initially understood in terms of infiltration of plume-related melts into the MORB plumbing system (4), but subsequent work found some E-MORBs far from plumes (5). A review of global MORB chemical distribution found that E-MORBs are unexpectedly more common and occur frequently at ridge segments not associated with plumes (3). The enrichment of highly incompatible elements and Nd-Sr-Hf-Pb isotope signatures evident in E-MORBs far from plumes is then explained by subduction and recycling of either MORB-like (6–10) or ocean island basalt–like pyroxenite (11, 12) or by refertilization of depleted peridotite by low-degree partial melts (13, 14) from subducted slabs. The two hypotheses predict distinct behavior in moderately incompatible elements, particularly elements that are sensitive to the amount of olivine versus clinopyroxene and/or garnet. The first-row transition elements (Sc-Zn), Ga and Ge (here termed the ScGe elements), have geochemical characteristics that span the compatible-incompatible range. Recent experimental and natural partitioning studies for these elements during mantle melting revealed the importance of Ge in assessing the role of pyroxenites since Ge was found to behave quite distinctly from Si between pyroxenite and peridotite melting (15, 16). We exploited the mineralogical preferences of ScGe elements to distinguish between these two hypotheses (15).

In this study and our former study (17), we analyzed 486 fresh MORB glasses from the Mid-Atlantic Ridge (MAR) (17), the Mid-Cayman Rise (MCR) (17), the East Pacific Rise (EPR), Endeavour ridge (18), and the Southwest Indian Ridge (SWIR) by laser ablation inductively coupled plasma mass spectrometry (LA-ICP-MS) for 60 elements, including Ge and Si measured on the same spot (table S1). We also analyzed a set of spinel peridotite xenoliths from San Carlos (AZ) for major and ScGe elements by LA-ICP-MS (table S2). MORB glasses analyzed here were assigned to lava flows (n = 264) following (19) (table S3). MORB lava flows were assigned to 24 ridge segments using discontinuities along the mid-oceanic ridges as boundaries (see the Supplementary Materials). MORB lava flows from each ridge segment were classified as D-MORBs with $(La/Sm)_N$ < 0.8, E-MORBs with $(La/Sm)_N$ > 1.5 (3), and N-MORBs as the intermediate compositions (fig. S1). Glasses from the MCR (17) and from the SWIR were treated as separate groups because of distinct geochemical features from other D-MORBs (see the Supplementary Materials). Glasses from E-MORBs analyzed in this study are from south of 15°20′ fracture zone (FZ) (MAR), Siqueiros FZ (EPR), and Endeavour ridge (EPR) (18), all far from plumes. Thus, these E-MORBs are ideal for the study of the enrichment of non-plume MORBs.

RESULTS

The method applied here simultaneously measures the abundances of about 60 elements in the same laser spot, including Si and Ge, transition metals (Sc, Mn, and Fe), high-field strength elements (e.g., Zr, Nb, Hf, and Ta), and rare earth elements (REE) (table S1). Precisely determining Ge in MORBs by LA-ICP-MS is challenging because MORBs are low in Ge [~1.6 parts per million (ppm)], and the Ge isotopes have molecular isobaric interferences principally from the plasma. We used a large laser spot size and high repetition rate to yield blank corrections <5% on the Ge peak with precision of ~±1% on the Ge abundance (see Materials and Methods). Repeated measurements of VG 2 and three U.S. Geological Survey (USGS) glasses during the course of analyses yielded a long-term precision of ±3% on Ge/Si (17). In striving for precise Ge abundances, we obtained precise elemental data for most elements of importance in this study [see (17) and Materials and Methods for further details]. The accuracy

[1]National High Magnetic Field Laboratory and Department of Earth, Ocean and Atmospheric Science, Florida State University, 1800 E. Paul Dirac Drive, Tallahassee, FL 32310, USA.
*Corresponding author. Email: humayun@magnet.fsu.edu

of our analyses was examined on the basis of the comparison of the analytical results of the MPI-DING glasses (17) and MORB glasses from this study with literature data (figs. S1 to S5 and see the Supplementary Materials).

To assess the effect of fractional crystallization on ScGe abundances, elemental abundances and key elemental ratios are plotted versus Mg# (fig. S2). During fractional crystallization, the abundances of Sc, Co, and Ge barely change, and the Ge/Si ratio stays constant as Mg# varies from 70 to 40 (fig. S2), so variations in the extent of fractional crystallization do not contribute to variability in the Ge/Si ratio. The abundances of Fe, Mn, Zn, and Ga change by tens of percent, and the Fe/Mn ratio increases by <5% during fractionation. Figure 1 (A and B) shows that the Ge/Si ratio in D-MORBs > N-MORBs > E-MORBs. Noticeably, D- and E-MORBs are well resolved. To assess whether this difference could also be observed in the only other MORB dataset to contain Ge abundances, Fig. 1 (C and D) compares the Ge/Si ratios in 99 MORB lava flows (see the Supplementary Materials) previously reported (20). These data are systematically ~8% lower than the data reported in this study (fig. S3 and see the Supplementary Materials), likely because of interlaboratory calibration issues, but this dataset also shows that most E-MORBs are systematically lower in Ge/Si (Fig. 1, C and D).

To corroborate whether the lower Ge/Si ratio is due to the presence of higher relative proportions of pyroxenite in the sources of E-MORBs, the abundance of Sc and the Fe/Mn ratios are also compared since both tracers are sensitive to the presence of garnet pyroxenite in the source (Fig. 1, E to H). Both Sc and Mn are preferentially retained in garnet-pyroxenite sources, so the contribution of partial melts from these sources would manifest as lower Sc and higher Fe/Mn ratios (15, 21). Figure 1 shows that E-MORBs are somewhat higher in their Fe/Mn ratios than D- and N-MORBs (Fig. 1, E and F) and correspondingly lower in their Sc abundances (Fig. 1, G and H). There are many datasets available for Sc abundances, but interlaboratory calibration issues inhibit the recognition of systematic differences. Thus, we compared three major sets of Sc abundances from literature sources (fig. S4) and found that E-MORBs are systematically lower in Sc than D-MORBs in each of these datasets. To quantitatively assess the differences between the MORB groups, frequency plots are shown for each of the three tracers (Fig. 1 and fig. S4), and E-MORBs are largely resolved from D-MORBs, with N-MORBs being intermediate in composition as expected.

There is a need for equally precise Ge abundances in mantle peridotites. Table S2 provides major and ScGe compositions for individual minerals measured on seven San Carlos spinel peridotites that are similar to MORBs in Sr, Nd, and Pb isotopes (22). Figure 2A shows that Ge is relatively uniformly (±10%, 1σ) distributed between the minerals of the seven xenoliths. Germanium abundances in orthopyroxenes and clinopyroxenes are analytically indistinguishable, and the relative distribution of Ge among the three minerals is consistent with experimental partitioning (15, 21) and recent measurements on natural systems (16). Bulk Ge abundances for peridotites were estimated by modal recombination of the mineral analyses (see the Supplementary Materials). Figure 2B shows that nearly all E-MORBs analyzed in this study have Ge/Si <6.5 × 10^6, while Ge/Si ratios of D- and most N-MORBs are above this value. The averaged compositions of D-, N-, and E-MORBs determined in this study clearly show that E-MORBs have higher Fe/Mn (Fig. 3A) but lower Ge/Si and Sc (Fig. 3B) relative to D- and N-MORBs, and E-MORBs are fully resolved from D-MORB when these elemental tracers were jointly applied (Fig. 3).

Relevant lithophile incompatible element ratios for MORBs analyzed in this study are provided in Figs. 4 and 5. Comparisons with literature data for element ratios or abundances are provided elsewhere ((17); see the Supplementary Materials). The Nb/Ta ratios in N- and E-MORBs are clearly higher than that of D-MORBs (Fig. 4). This effect is also observed in various literature compilations, although interlaboratory calibration issues have smeared out the signal seen clearly in data from a single laboratory (fig. S5). Low-degree partial melts of pyroxenite have high Nb/Ta ratios due to the selective retention of Ta by clinopyroxene in the source (fig. S6). Criteria for recognizing pyroxenite contributions during mixed-lithology melting from incompatible elements (23) indicate that elemental ratios of La/Nb, (La/Yb)$_N$, Zr/Pb, and Ba/La should discriminate pyroxenite melts derived from recycled MORB or recycled MORB and continental sediment or delaminated lower continental crust (LCC) from spinel or garnet peridotite melts. The (La/Yb)$_N$ ratio is substituted by the (Sm/Nd)$_N$ ratio, and the (La/Sm)$_N$ and Rb/Sr ratios are added. Figure 5 (A, B, and D) shows that the Ba/La, La/Nb, and Rb/Sr ratios behave similarly to Nb/Ta ratios in that D-MORBs plot systematically higher or lower than N- and E-MORBs. The ratios (La/Sm)$_N$, (Sm/Nd)$_N$, and Zr/Pb tend to discriminate the three groups better (Fig. 5, C, E, and G). The presence of continental material with its high Pb content tends to lower the Zr/Pb ratio, making this ratio an excellent indicator of recycled continental crustal material in the source. Thus, Fig. 5C indicates that recycled continental material is present in the sources of E-MORBs > N-MORBs > D-MORBs. Glasses from the SWIR have the lowest Zr/Pb ratios (Fig. 5C) and anomalously high Pb/Ce and Tl/Ce (not shown) ratios for MORB, although their (La/Sm)$_N$ ratios imply a depleted source (fig. S1). The Ge/Si ratios of the SWIR glasses are consistent with melting of a peridotite source fertilized by continental material, as exemplified by the discovery of Jurassic zircons from the same FZ (24). The higher Zr/Pb and lower (Sm/Nd)$_N$ of MCR glasses is likely due to the lower degree of melting compared with other D-MORB (25).

DISCUSSION

The fundamental observations made here that E-MORBs have lower Ge/Si, higher Fe/Mn, and lower Sc abundances, in addition to being enriched in incompatible elements, imply a role for pyroxenite melts. Elemental abundances that effectively discriminate pyroxenite melts from peridotite melts have to be sensitive to the distinctive mineralogy of pyroxenites (garnet and clinopyroxene) or to the distinctive effects experienced by slab crust: alteration (e.g., Ba/La and Rb/Sr), sediment addition (e.g., Zr/Pb), and passage through the subduction factory (e.g., La/Nb). Mineralogical controls influence the Ge/Si, Fe/Mn, and Nb/Ta ratios and Sc abundances because of the compatibility of Ge, Mn, and Sc with garnet (fig. S6, A, E, and F) and clinopyroxene's preference for Ta over Nb (fig. S6H). The partitioning ($D^{mineral-melt}$) of Si, Sc, Mn, Fe, and Ge has been well constrained for peridotite melting (15, 21), showing that Ge is slightly incompatible in olivine, neutral (D~1) in pyroxenes, and compatible in garnet (fig. S6). Similar results have been obtained on natural peridotites (16). Germanium partitions onto the tetrahedral site of pyroxenes so that D_{Ge} in clinopyroxene and orthopyroxene is essentially identical (Fig. 2A and fig. S6F), and the M-site occupancy has little effect on D_{Ge} in pyroxene. Application of these principles to discriminating pyroxenite and peridotite melts is developed below for the ScGe elements, while other tracers used here have been developed in (23).
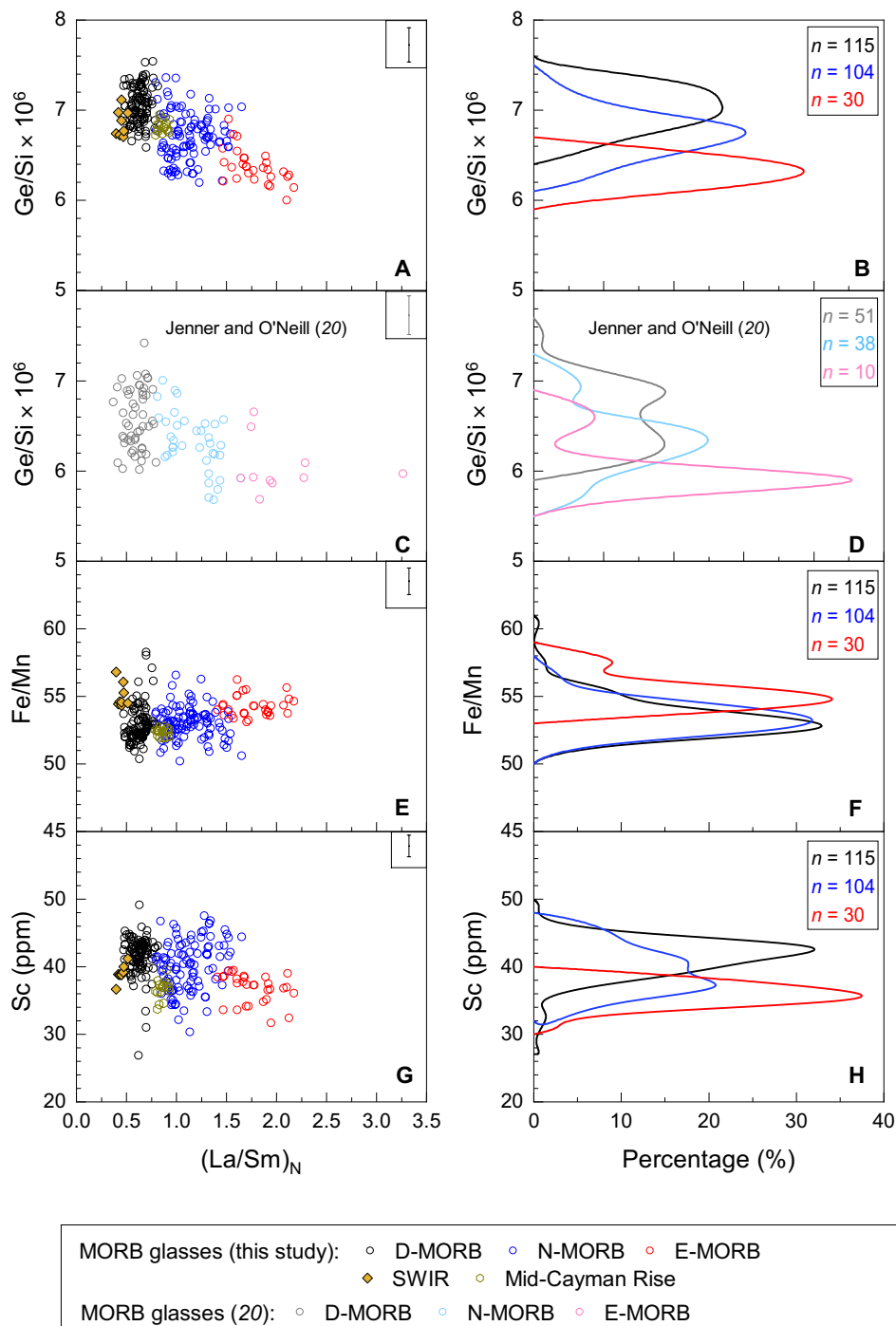
Fig. 1. Elemental indicators of pyroxenite in the MORB source and their associated frequency plots: (**A** and **B**) $Ge/Si \times 10^6$ (this study), (**C** and **D**) $Ge/Si \times 10^6$ (20), (**E** and **F**) Fe/Mn, and (**G** and **H**) Sc. The Ge/Si data of (20) are systematically offset from data in this study (fig. S3) and hence were shown separately. The black line (this study) and the gray line (20) represent separate datasets. In Fig. 1B, MCR glasses were not included in calculation of the black line, but SWIR glasses are included. A representative analytical error bar (±1σ) for these ratios is presented in the insets. MORBs groups are defined in fig. S1, color-coded as follows: black, D-MORB; blue, N-MORB; red, E-MORB; brown diamonds, D-MORBs from SWIR; gold circles, MCR. The numbers of D-, N-, and E-MORB lavas are given in the insets of the histograms. This color coding is used consistently throughout this manuscript.

Germanium-silicon geochemistry of MORBs

Partial melting of MORB-like pyroxenite (eclogite), or secondary pyroxenite derived from reaction of eclogite-derived melt with peridotite, is known to create liquids that are more SiO_2 rich than partial melts of mantle peridotite (9, 10). Si-deficient pyroxenites yield melts that are lower in SiO_2 compared with melts of MORB-like pyroxenites (26). Arclogites are expected to have similar Ge-SiO_2 compositions to MORB, but there are no experimental melt compositions
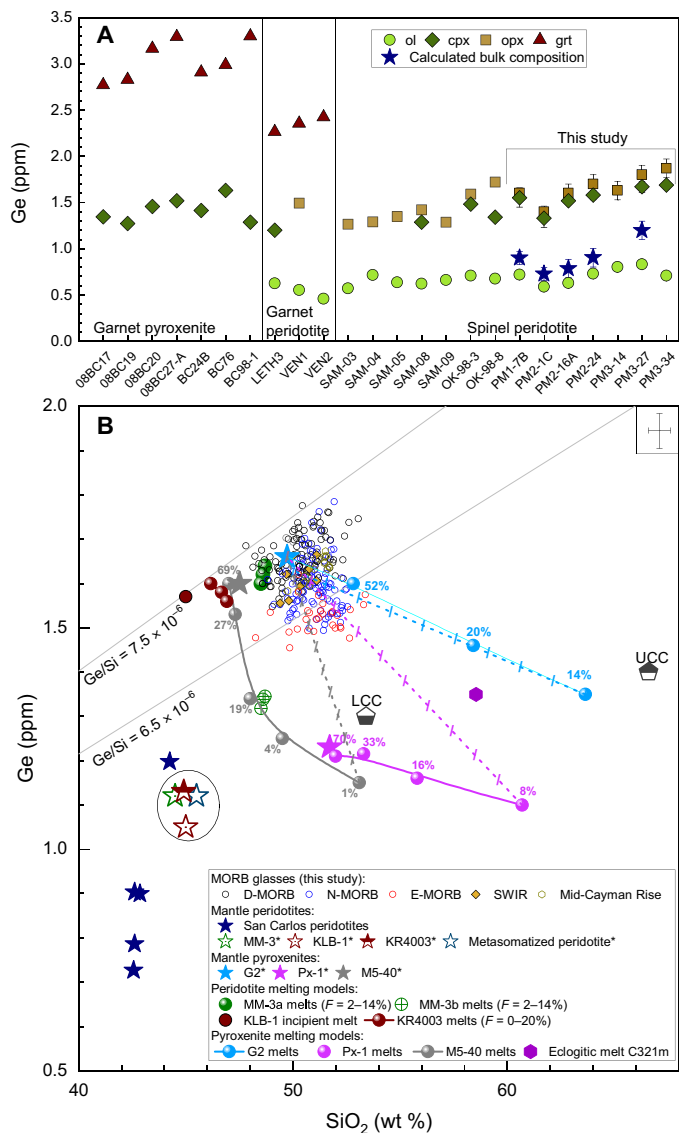
Fig. 2. Germanium-silicon geochemistry of mantle peridotites, pyroxenites, and melts. (**A**) LA-ICP-MS analyses of Ge abundances in minerals from San Carlos mantle xenoliths (PM, this study) and of Ge in minerals from peridotites and pyroxenites (16). Calculated bulk Ge abundances in five San Carlos mantle xenoliths (see the Supplementary Materials) are also shown. (**B**) Germanium-silica relations of MORB glasses and mantle peridotites (this study) compared with predictions from melting models of a two-lithology mantle (see the Supplementary Materials). Inset shows a representative analytical error bar (±1σ) for Ge and SiO_2, and gray lines show constant Ge/Si ratio labeled with their Ge/Si ratios. Source compositions are shown as stars; upper continental crust (UCC) and lower continental crust (LCC) from (32). Mixing lines between D-MORB and low-degree pyroxenite melts shown with a mixing interval of 10%. For both peridotite and pyroxenite melting models, melt SiO_2 contents and mineral and melt proportions were taken from the original experimental studies (9, 10, 26, 28–30). Peridotite metasomatized by low-degree slab melts (13) is shown as the teal star. Melts from silica-excess pyroxenite are known to be high in SiO_2 but have modeled Ge contents that plot at low Ge/Si because of compatibility of Ge in garnet (grt) and clinopyroxene (cpx). ol, olivine; opx, orthopyroxene.

currently available (27). To explore the effects of two-lithology mantle (peridotite versus pyroxenite) on the Ge-SiO_2 composition of MORBs, melting and mixing models were built with silica-excess MORB-like
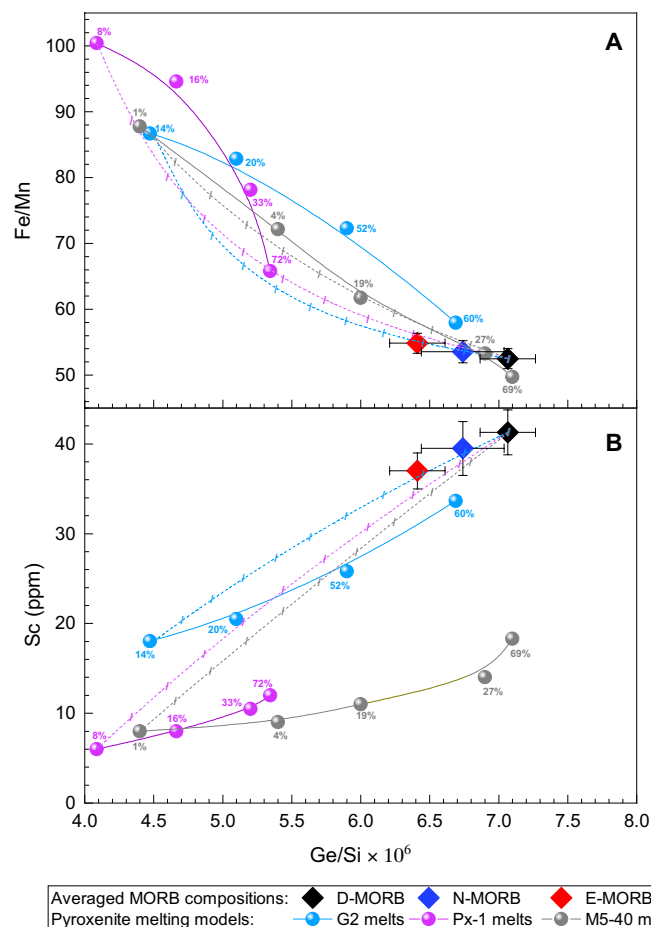

Fig. 3. Comparison of averaged MORB compositions with mixing models between average D-MORB and pyroxenite melts. Plot of Ge/Si × 10^6 versus (**A**) Fe/Mn and (**B**) Sc in averaged D-, N-, and E-MORB compositions. SWIR D-MORBs are not included when calculating the averaged composition of D-MORBs analyzed in this study (see the Supplementary Materials). Error bars indicate the 1σ SDs of the averages. Pyroxenite melt compositions as a function of melt fraction (labeled) are shown for three representative cases. The major element compositions (SiO_2, FeO_T, and MnO) of pyroxenite melts were taken directly from the experiments (9, 10, 26), while Ge and Sc contents of pyroxenite melts were calculated (see the Supplementary Materials). Mixing trends are between D-MORB magma and low-degree melts from the three pyroxenitic sources, with 10% mixing interval indicated. Mixing of silica-excess pyroxenite (9, 10, 26) melts successfully reproduces the observed correlations of Ge/Si against Fe/Mn (A) and against Sc (B).

pyroxenite G2 (10), secondary pyroxenite Px-1 (9), and silica-deficient pyroxenite M5-40 (26), as well as spinel peridotite MM-3 (28) and garnet peridotites KLB-1 and KR4003 (29, 30) starting compositions. Figure 2B shows a plot of Ge versus SiO_2 for MORBs compared with model predictions. To understand how Ge behaves during partial melting, fig. S6F compiles the known experimental partition coefficients for Ge and Si during spinel or garnet peridotite melting (15, 21). There currently are no partition coefficients available for garnet and clinopyroxene for Ge in pyroxenite compositions, so that Ge partitioning during pyroxenite melting had to be inferred from peridotite partitioning data for garnet and clinopyroxene (Fig. 6F). As a major element, SiO_2 abundances had to be obtained from experimental melt and mineral compositions for pyroxenites (9, 10, 26) and for spinel and garnet peridotites (28–30).
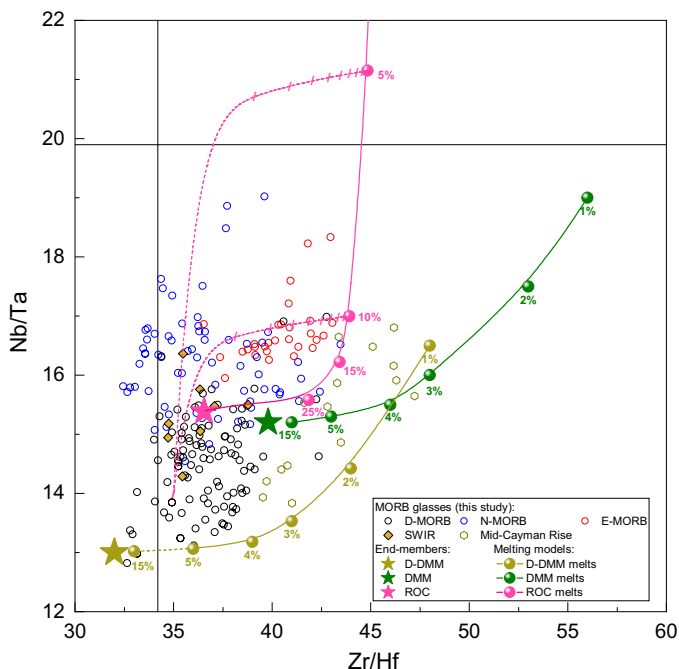
Fig. 4. Correlation of Nb/Ta against Zr/Hf in MORB lavas analyzed in this study compared with modeled melting curves of two spinel peridotite compositions (brown and green curves) and pyroxenite (pink curve) with horizontal and vertical lines representing chondritic values (60). Note that these models, based on (23), are distinct from models shown in Figs. 2 and 3 and are shown with a new set of color-coded curves. Sources for the high-field strength element compositions of recycled MORB (pink star), DMM (green star), and D-DMM (brown star), and experimental partition coefficients (Ds) are in the Supplementary Materials (table S4 and fig. S6). Mixing lines are drawn between a D-MORB composition (table S4) and low-degree partial melts ($F = 5$ and 10%) derived from recycled MORB, with 10% mixing intervals. Garnet peridotite melting is not shown since it yields a curve essentially identical to that of spinel peridotite melting. The larger incompatibility of Nb and Ta results in relatively little change in the Nb/Ta ratio in a mixing scenario compared with the Zr/Hf, explaining why E-MORBs have similar Nb/Ta ratios to N-MORBs but higher than D-MORBs.

The Ge abundances for the starting compositions were obtained as follows: Minerals from San Carlos spinel peridotites (Fig. 2A) were taken to represent typical mantle mineral abundances that were then applied to experimental starting compositions using mineral modes. This produced Ge contents of ~1.1 ppm, which complemented known SiO_2 abundances, for spinel peridotite MM-3 (28) and for garnet peridotites KLB-1 (29) and KR 4003 (30), which are similar to Ge estimated for primitive mantle (PM) (31) and DMM (2), indicating that Ge abundances in fertile peridotite starting compositions are not subject to much variability (Fig. 2B). Melt depletion results in higher modal olivine and lower Ge contents, but more depleted peridotites are still in equilibrium with melt Ge contents of ~1.6 ppm as the bulk D_{Ge} inversely varies with the olivine modal abundances (see the Supplementary Materials). The Ge contents for experimental spinel peridotite melts were calculated using experimental modes of MM-3 (28) and partition coefficients (15, 21) to produce the melt compositions shown in Fig. 2B. Spinel peridotite melt compositions ($F_L = 2$ to 14%) obtained using the partition coefficients in (15), labeled MM-3a, yielded Ge abundances compatible with D-MORBs, while the higher D_{Ge} in (21) yielded melt compositions, MM-3b, that are too low in Ge

(1.3 ppm) for any MORB. The degree of melting has little effect on Ge abundances in partial melts since Ge is sufficiently compatible to be in the 1/D limit. The garnet peridotite melt compositions for KLB-1 (29) and KR4003 (30) yield Ge/Si ratios similar to D-MORB at lower SiO_2 (and Ge) abundances (Fig. 2B). This provides a validation of both the partition coefficients (15) and the mantle Ge abundances used here.

The Ge abundance for recycled MORB-like pyroxenite G2 (blue star, Fig. 2B) was taken as the average Ge of D-MORB (1.66 ppm) obtained in this study. The Ge abundance for silica-deficient pyroxenite M5-40 (gray star, Fig. 2B) was calculated assuming that the Ge/Si ratio of M5-40 is the same as the average Ge of D-MORB. The Ge content of secondary pyroxenite Px-1 (purple star, Fig. 2B) was obtained by mixing peridotite with eclogite-derived melt (9). The Ge contents for partial melts for all three pyroxenite compositions were calculated using available garnet and clinopyroxene partition coefficients with experimentally determined major element compositions (see the Supplementary Materials). Low-degree partial melts of all three pyroxenite compositions are inferred to have lower Ge/Si relative to D-MORB (Fig. 2B). Since $D_{Ge} \sim 1$ in pyroxene (fig. S6F), the melting of eclogite with pyroxene as the sole residual phase will produce melts with Ge similar to D-MORB but with higher SiO_2 contents (9, 10, 26). Since Ge is compatible in garnet (fig. S6F), the presence of garnet in the low-degree melting residue of MORB-like pyroxenite G2 (10) reduces Ge contents in the melts relative to that in D-MORB (blue curve, Fig. 2B). Modeled partial melts of secondary pyroxenite Px-1 (purple curve, Fig. 2B) (9) have even lower Ge contents because the hybrid source has lower initial Ge content (see the Supplementary Materials), higher proportions of garnet (9), and is more mafic (9) (lower SiO_2) than MORB-like pyroxenite (10). Low-degree (<5%) partial melts of Si-deficient pyroxenite M5-40 (gray curve, Fig. 2B) have low modeled Ge contents and low SiO_2 contents (26). Mixtures of low-degree partial melts of all three pyroxenites and D-MORB plot to lower Ge/Si ratio due to Ge retention in the garnet-clinopyroxene residues (Fig. 3). Mixing of ~10 to 30% low-degree pyroxenite melts into D-MORB–like melts explains the lower Ge/Si in E-MORBs. Despite the many assumptions that go into the models, the models robustly capture the fact that pyroxenite partial melts, while high in SiO_2, have to have lower Ge/Si ratios than their starting compositions (e.g., D-MORB). Using Ge partitioning in natural samples, He *et al.* (16) also found that pyroxenite melts would have low Ge/Si ratios. The continental crust is silica rich but has low Ge/Si ratios (32) similar to pyroxenite partial melts (Fig. 2B). The origin of the high Si in upper continental crust (UCC) is likely far more complex than direct derivation from eclogite (16), but the role of eclogite melting in the formation of Archean crust (33) likely contributed to the low Ge/Si of both UCC and LCC, which could not have been accomplished by internal differentiation of the crust alone.

The metasomatized peridotite model (13) calls for ultralow-degree ($F_L = 1\%$) slab melts to metasomatize a large volume of mantle wedge, forming a peridotite source enriched in incompatible elements, which is subsequently melted under the ridges to form E-MORB. This model explains enrichments in incompatible element abundances observed in E-MORBs relative to N-MORBs (13), since an ultralow-degree melt effectively enriches the incompatible elements without perturbing major and compatible element abundances. Because of the low degree of melting invoked and the compatibility of Ge (and Si), the metasomatized peridotite (13) (teal star, Fig. 2B) formed by this process (see the Supplementary Materials) has almost identical Ge and
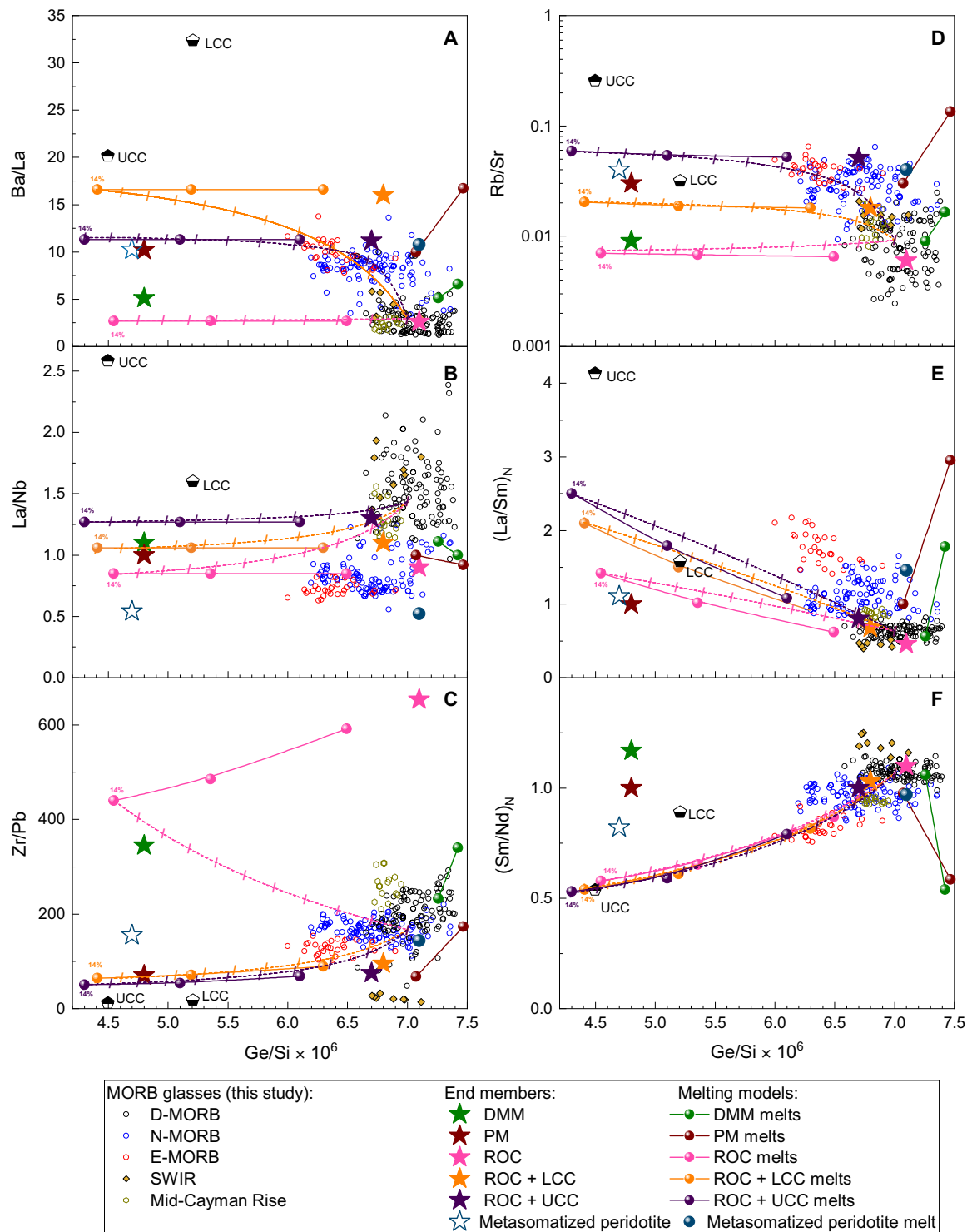
Fig. 5. Correlations of selected elemental tracers versus Ge/Si ratios of MORB compared with predictions of various sources and melting models (13, 23, 39). Ratios of (**A**) Ba/La, (**B**) La/Nb, (**C**) Zr/Pb, (**D**) Rb/Sr, (**E**) (La/Sm)$_N$, and (**F**) (Sm/Nd)$_N$ are plotted against Ge/Si ratios. The melting models and parameters in (13, 23) were used to calculate the elemental ratios in modeled melts (see table S4). Three melting models of pyroxenites are shown: ROC (23) (pink), a mixture of ROC (85%) and LCC (15%) (23) (orange), and a mixture of ROC (95%) and UCC (5%) (violet). Mixing curves (pink, orange, and violet dashed lines) are between low-degree pyroxenite melts (F = 14%) and the average D-MORB composition at 10% mixing increments (table S4). Melting models and source compositions of peridotite compositions are shown for DMM (2) (green); PM (31) (burgundy); and metasomatized peridotite (13) (teal). The ratios of Ge/Si of modeled melt compositions are taken from Fig. 2B. Mixing of D-MORB with peridotite melts defines vertical arrays of data (i.e., constant Ge/SiO$_2$), while mixing of D-MORB with pyroxenite melts accounts for the observations (except in Fig. 5E).
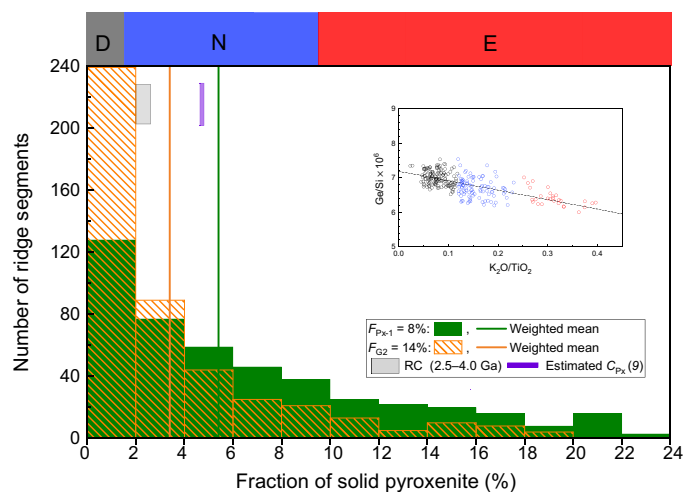
Fig. 6. The estimated proportions of solid pyroxenite (in percentage) are shown as a function of frequency in the mantle sources of 447 global MORB segments estimated from the correlation of Ge/Si ratio with K_2O/TiO_2 ratio in MORBs. Separate histograms are shown for choices of 8% (solid green, Px-1) and 14% (orange stipple, G2) degrees of melting of pyroxenites (F_{Px}) (see the Supplementary Materials). The approximate correspondence of the D-MORB, N-MORB, and E-MORB fields were transposed on this figure from the relationship between Ge/Si and K_2O/TiO_2 (inset, see the Supplementary Materials). The vertical lines correspond to weighted means by segment of the amount of recycled crust estimated in the global MORB source for the two C_{Px} estimates (green and orange lines). The weighted mean of the C_{Px} in our study brackets an independent estimate from (9) (purple box). The gray box shows a range for the amount of the recycled crust (RC) created over time with uniform production from 2.5 or 4.0 Ga ago to the present (see the Supplementary Materials).

SiO_2 composition to that of the original peridotite and thus cannot yield the lower Ge/Si observed in E-MORB. To form a suitable mantle source to yield the Ge/Si of E-MORB without invoking pyroxenite melts, the model would need to lower the Ge content of the peridotite source by ~10 to 15%. Even if the hypothesized slab melts had no Ge, a minimum of 10 to 15% slab melt would need to be added to lower the Ge/Si ratio of the mantle sufficiently to yield E-MORB compositions. Thus, the modest amounts of metasomatic melt in the mixture (0.5%) called for by the metasomatized peridotite model (13) cannot perceptibly leverage the Ge/Si ratio. The metasomatized peridotite model (13) also fails to explain the lower Sc contents and higher Nb/Ta and Fe/Mn ratios observed in E-MORBs relative to D-MORBs.

Corroborative evidence for the presence of pyroxenite melt in MORB sources

While pyroxenites have long been proposed as part of the MORB source (34, 35), their chemical signatures have been indirectly inferred from incompatible element isotopic ratios or elemental abundances (14, 23, 35). Direct major element contributions have proven very hard to assess (26). To corroborate our findings, we examined a number of other tracers [Sc, Fe/Mn (36), Nb/Ta, Ba/La, La/Nb, and Zr/Pb] analyzed in the same glasses that are sensitive to the presence of pyroxenite melt (23). We also examined the Rb/Sr, $(Sm/Nd)_N$, and $(La/Sm)_N$ ratios to see whether the enrichments in incompatible elements could also be attributed to pyroxenite melting. Figure 1 shows that the Fe/Mn ratio is higher, while the Sc abundances are lower, in

E-MORBs that exhibit lower Ge/Si ratios consistent with the role of pyroxenite melts. Figure S2 shows that the Sc contents (fig. S2A) and Fe/Mn (fig. S2C) ratios are not meaningfully affected by fractional crystallization in MORB. To reveal systematic chemical differences between the various types of MORB, each MORB group was separately averaged. The averaged Fe/Mn ratios anticorrelate with the averaged Ge/Si ratios (Fig. 3A), while the averaged Sc contents correlate with the averaged Ge/Si ratios (Fig. 3B). The addition of silica-excess pyroxenite melts to D-MORB melt successfully explains the observed covariation with low-degree (<15%) melts from either MORB-like pyroxenite G2 (10) or from secondary pyroxenite Px-1 (9) (Fig. 3). Silica-deficient pyroxenite M5-40 melts (26) are too high in Fe/Mn (Fig. 3A) and too low in Sc (Fig. 3B) at a given Ge/Si to explain the observed trends. These models show that for melts from silica-excess pyroxenites, the impact on Ge/Si is larger than on Fe/Mn (Fig. 3A) and similar on Sc (Fig. 3B). Thus, the addition of 25 to 30% of low-degree (8 to 14%) partial melts from pyroxenite to a D-MORB–like composition is sufficient to obtain the ~14% lower Ge/Si while increasing the Fe/Mn by ~7% (Fig. 3A) and decreasing Sc by 13% (Fig. 3B) as observed for average E-MORB. Thus, while pyroxenite signatures are less apparent in Fe/Mn than in Ge/Si and Sc between D-MORB and E-MORB, the effects are resolved. These findings are not specific to the type of pyroxenite used, as long as melts from these pyroxenites have garnet and clinopyroxene on their liquidus.

Both Nb and Ta are highly incompatible elements, more incompatible than Zr and Hf, but Ta is relatively more compatible in clinopyroxene than Nb (fig. S6H). The Nb/Ta ratios of low-degree melts of recycled oceanic crust [ROC; (23)] (pink star, Fig. 5) are higher than that of their source for F_L < 15 to 20% (pink curve, Fig. 5). The Nb/Ta ratios of low-degree peridotite melts are higher than that of their source for F_L < 3% as well (see the Supplementary Materials). Mixing lines between low-degree pyroxenite melts and a D-MORB composition show that 10 to 30% admixing of pyroxenite melt into a D-MORB would change the Zr/Hf ratio while keeping the Nb/Ta ratio similar to that in the pyroxenite melt. While adding variable amounts of low-degree pyroxenite melts into D-MORB explained the D > N > E sequence observed in Ge/Si ratios of MORBs, the incompatibility of Nb and Ta results in N- and E-MORB having similar Nb/Ta ratios (Fig. 4), both distinct from that of D-MORB. Figure 4 also explains why D-MORBs have such a large range in Nb/Ta ratios: Extraction of small amounts of melt from a peridotite will lower the Nb/Ta ratio of the depleted residue. The findings arrived at here are independent of the exact Nb/Ta (or Zr/Hf) ratios chosen for the source compositions (Fig. 4), although the emphasis placed here on pyroxenite melt mixing is justified since low-degree peridotite melts would not explain the Ge/Si, Fe/Mn, and Sc evidence that motivated this discussion. Individual pyroxenites have wide ranges of Nb/Ta ratios, but even averaged arclogites (27) have similar Nb/Ta ratios to ROC (23).

Now that it has been shown that the ScGe tracers and Nb/Ta ratios of MORBs reflect the presence of pyroxenite mineralogy in the source, other tracers that reflect the processing of recycled oceanic crust through subduction zones need to be assessed here. Stracke and Bourdon (23) elegantly summarized the incompatible element ratios that effectively trace melts from recycled oceanic crust that we apply here to the variations observed in MORBs (see the Supplementary Materials). Figure 5 shows that these incompatible trace element ratios in MORBs are consistent with mixtures between low-degree melts from ROC with

D-MORB. Melts of garnet peridotite (PM, burgundy star), spinel peridotite (DMM, green star), and two varieties of recycled oceanic crust, recycled MORB (ROC) that has been altered and dehydrated in a subduction zone (pink star), and ROC mixed with 15% LCC (orange star) are shown with their melting trends and mixing lines in Fig. 5 (see the Supplementary Materials). The use of the Ge/Si ratio as the abscissa (x axis) introduces a nonintuitive aspect to Fig. 5: Melts of pyroxenite have lower Ge/Si than that of their sources (assumed to be D-MORB–like), while melts of peridotite have higher Ge/Si than that of their sources. Because of the need to obtain SiO_2 abundances from experimental data, the degree of melting for modeling incompatible elements is taken at the experimentally determined melt fractions as used in the melting models for MORB-like pyroxenite G2 (see the Supplementary Materials). The ratios of highly incompatible elements (Ba/La and La/Nb) have converged to that of their sources by 14% melt fraction, the lowest experimentally determined melt fraction for MORB-like pyroxenite G2 (*10*). Like for Nb/Ta, N- and E-MORBs group together because of the fact that a low-degree partial melt of pyroxenite effectively dominates the Ba/La or La/Nb ratios of the mixed melt. This aspect of the models is observed from the flattening of the mixing lines >30% mixing (Fig. 5, A and B).

Figure 5 confirms that peridotite partial melts cannot explain the variations observed between D- and E-MORBs because any mixing trends would be vertical, e.g., the Ba/La ratio of the peridotite source would be variable, but the Ge/Si ratio of the peridotite melts would remain constant. The Rb/Sr, Ba/La, and Zr/Pb ratios indicate that the recycled oceanic crust had to have some continental material admixed into the pyroxenite source (Fig. 5, A, C, and D). Since fluid-mobile elements (Rb, Sr, Ba, and Pb) are stripped from recycled crust by subduction zone processes [e.g., in (*37*, *38*)], sufficient excess Rb, Ba, and Pb had to be initially present to retain high Rb/Sr and Ba/La and low Zr/Pb in the recycled crust after subduction. In this regard, it is worth noting that stable Ba isotopes indicate the presence of a recycled marine sediment component in E-MORB (*39*). To assess the presence of sediment in the subducted crust, partial melts (14 to 52%) and their mixing lines of a new composition consisting of 95% ROC and 5% UCC (violet star, Fig. 5) are shown in Fig. 5. The amount of UCC used (5%) is determined by the need to fit the Rb/Sr ratio of E-MORB at F_L of 14%, but is 50 times higher than that needed to explain the Ba isotopes (*39*), which used the global subducted sediment [GLOSS; (*40*)] composition. The GLOSS composition has a higher Ba/La ratio but a lower Rb/Sr ratio, so that the failure of any of the three models to explain the Rb/Sr enrichment of E-MORBs implies that either lower degree melts of the pyroxenite are required or another process (perhaps aqueous fluids) must be invoked to increase the Rb/Sr ratio of the source. Similarly, the magnitude of the $(La/Sm)_N$ ratio at any Ge/Si ratio cannot be fit with any of the three pyroxenite models at 14% melting nor by the metasomatized peridotite model (*13*), because peridotite melts exhibit constant Ge/Si ratios.

The Zr/Pb ratio for SWIR D-MORBs is not consistent with pyroxenite addition but requires a metasomatized peridotite source enriched in Pb since the SWIR glasses plot to low Zr/Pb at Ge/Si ratios of D-MORB (Fig. 5C). By contrast, none of the three pyroxenite sources evaluated had a sufficiently low La/Nb ratio to account for the pyroxenite end-member (Fig. 5B). The models successfully fit the $(Sm/Nd)_N$ ratio for all three compositions chosen because this ratio reflects the presence of a garnet-rich pyroxenite source. A garnet peridotite melt would move the mixing line vertically downward and cannot explain the observed data (Fig. 5F). Any tendency toward

linear variations between incompatible element ratios and Ge/Si ratios in Fig. 5 is limited by the chemical variability in the E-MORB localities of this study, as N-MORB tend to show greater diversity but are harder to distinguish in Ge/Si from D-MORB. Much work remains to understand the nature and diversity of the pyroxenite components in MORB other than D-MORB.

Last, the mixing of low-degree pyroxenite melt (8 to 14%) with 7 to 11% partial melting of peridotite is only conceivable if the pyroxenite solidus is close to the peridotite solidus, which is not the case for G2, the best-studied pyroxenite (*10*). It is important to emphasize here that the solidi for pyroxenites exhibit a wide range from near peridotite solidi to >200°C lower (*10*, *41*, *42*). Any pyroxenite composition that has either clinopyroxene or clinopyroxene and garnet on its liquidus will produce low-degree partial melts with low Ge. The mixing relations in the ScGe data provide a constraint on the average differences between the solidi of pyroxenites and peridotites in MORB mantle.

Estimating the amount of recycled crust in the sources of global MORBs

The chemical tracers used above consistently show that much of the incompatible element enrichment observed in E-MORBs can be explained by the addition of low-degree partial melt (F_{Px} ~8 to 14%) of recycled oceanic crust to D-MORB–like melts. Combining the Ge/Si, Fe/Mn, and Sc data (Fig. 3) allows the calculation of the amount of solid pyroxenite (C_{Px}) that is melted (see the Supplementary Materials). Solving the mass balance equation for the amount of solid pyroxenite in the source requires knowledge of the degree of melting of the peridotite (F_{Pe}) that we took to be 7 to 11% (see the Supplementary Materials). In Fig. 6, we calculated the spectrum of solid pyroxenite (C_{Px}) in the mantle sources of MORBs for values of F_{Px} 8 or 14%. We assumed that the source of average D-MORB is devoid of pyroxenite. The requirement of finding a large amount of low-degree pyroxenite melt depends on the amount of solid, recycled crust in the mantle source and on whether MORB-like pyroxenite G2 (*10*) or secondary pyroxenite Px-1 (*9*) is invoked, a choice that cannot be discriminated on the basis of our data. The minimum amount of solid recycled MORB-like pyroxenite (*10*) in a peridotitic (DMM) source required to produce E-MORB is ~10%, while that of the solid primary eclogite (*9*) precursor to secondary pyroxenite (*9*) required to produce E-MORB is 16% (see the Supplementary Materials). For N-MORB compositions, intermediate amounts are required (see the Supplementary Materials). This conclusion would need to be modified if partial melt compositions for arclogites turn out to be different from that of MORBs.

Next, we estimated the global distribution of recycled crust in the mantle sampled at ridges. The MORB glasses analyzed span the Pacific, Atlantic, and Indian oceans and exhibit the same chemical variability (e.g., K_2O/TiO_2 = 0.0 to 0.4) in this sample set that is observed in the majority (447 of 465) of global MORB ridge segments (*3*). A generalized relationship between K_2O/TiO_2 and Ge/Si was established for the measured MORB glasses (Fig. 6 inset) from which we calculated the amount of solid pyroxenite in the sources of a global set of averaged segment compositions of MORB (*3*) (Fig. 6 and see the Supplementary Materials). While this calculation is no substitute for direct measurement, Fig. 6 illustrates the power of the technique that we have developed to quantify the amount of recycled oceanic crust in the sources of basalts. At F_{Pe} 7%, the mode for recycled crust in MORB mantle is only ~0 to 2%, and the global average is ~4 to 6% (Fig. 6), compared with ~2 to 3% recycled oceanic crust created over time

with uniform production since 2.5 to 4.0 billion years (Ga) ago (43–45) (see the Supplementary Materials). The estimated C_{Px} in Fig. 6 will be lower if MORB sources have a significant amount of refractory peridotite that is not involved in basalt genesis during melting at ridges (46–48). The amount of such refractory peridotite in the MORB source constrained from Nd-Hf isotope correlations ranges from 0 to 50% (47, 48), implying that the actual amount of solid pyroxenite in the source may be lower by a factor of ~2 than shown in Fig. 6. When this adjustment for refractory peridotite is made, the estimated amounts of C_{Px} do not exceed plausible limits on the amount of crust produced over time (2 to 3%) and agree with an independent estimate (9). This distribution (Fig. 6) explains why E-MORBs far from plumes are so abundantly sampled at ridges (3).

The ScGe elemental abundances combined with Nd-Hf isotopes provide a powerful technique with which to test geological assumptions of the amount of oceanic crust subducted over time. Thus, models of plate recycling that initiate subduction at ~1 billion years ago (49) produce too little recycled crust (<1%) to explain the constraints imposed by our data (Fig. 6).

The findings arrived at here depend importantly on the partition coefficients of ScGe elements between melts and residues and on the pyroxenite composition. There are enough available partitioning studies with which to model peridotite melting, although we noted contradictions between the two studies (15, 21), but there are no available partitioning experiments for pyroxenite melt compositions. Delaminated lower arc crust might also involve a role for hornblende (50), a mineral with Ge-Si exchange partition coefficients similar to that of garnet (16). Thus, future experimental studies of ScGe partitioning between various pyroxenite compositions for recycled crust, arclogites, Archean crustal analogs, etc., and their partial melts are going to be essential in reliably interpreting the constraints that ScGe abundances provide on the amount of recycled crust in the mantle beneath ridges.

MATERIALS AND METHODS

Fresh MORB glasses ($n = 486$) from the MAR ($n = 289$), MCR ($n = 30$), EPR ($n = 108$), Endeavour ridge ($n = 44$), and SWIR ($n = 15$) were analyzed using LA-ICP-MS in this study. All MORB glasses from MAR and MCR were obtained from the Smithsonian Seafloor Rock Collection. An LA-ICP-MS dataset including the contents of the 60 elements in these glasses is available in (17). EPR glasses analyzed in this study are a part of the dredged samples collected by the CHEPR cruise (51) and by the PANORAMA cruise, covering the ridge segments of EPR between 6°N and 18°N. Eight glasses from the Siqueiros FZ were dive samples from the Atlantis-II 125-25 Research Cruise (55). The SWIR samples analyzed in this study were collected between 48°50′E and 50°29′E along SWIR by the research vessel *Dayang Yihao*, covering the ridge segment between Indomed FZ and Gallieni FZ (52).

MORB glasses analyzed in this study (table S1) were assigned to 264 MORB lava flows based on the homogeneity of major element analyses following (19). The lava flow group number (table S3) for MAR samples is taken from (19); for EPR and SWIR, samples are assigned in this study following (19); and for Endeavour, samples are taken from (18). MORB lavas from each ridge segment are grouped into D-, N-, and E-MORBs (fig. S1). MORBs with $(La/Sm)_N > 1.5$ are E-MORBs while with $(La/Sm)_N < 0.8$ are D-MORBs (3); MORBs that are neither D- nor E-MORBs were designated as N-MORB (17).

MORBs with $(La/Sm)_N$ ratios that are close to the "cutoff" values were grouped the same as most of the samples from this segment (17). Although SWIR MORBs analyzed in this study have $(La/Sm)_N$ and K_2O/TiO_2 ratios that both fall in the D-MORB category (fig. S1), they are distinct from other D-MORBs analyzed in this study in many trace elemental ratios (e.g., Pb/Ce, Tl/Ce, and Nb/U).

A full description of analytical methods, including operation conditions of ICP-MS, laser ablation parameters, mass peaks acquired, isobaric interference correction, and selection of external calibration materials are given in (17) and will be briefly summarized here. This section will mainly focus on our technique of measuring Ge precisely (±1%) as determining Ge in MORBs by LA-ICP-MS is challenging because MORBs are low in Ge (~1.6 ppm), and the Ge isotopes have molecular isobaric interferences principally from the plasma.

All samples were measured on a magnetic sector, single-collector, Thermo Element XR ICP-MS coupled to an Electro Scientific Instruments New Wave UP-193FX ArF (193 nm) excimer laser ablation system at the Plasma Analytical Facility of the National High Magnetic Field Laboratory, Florida State University (17, 53–55). Mass peaks acquired are given in table S1. One of the initial purposes of this study was to precisely measure Ge (±1%), which required selecting laser spot size and repetition rate to yield the least blank contribution. Germanium has five isotopes: ^{70}Ge (20.5%), ^{72}Ge (27.4%), ^{73}Ge (7.8%), ^{74}Ge (36.5%), and ^{76}Ge (7.8%), in which ^{72}Ge is interfered by ^{36}Ar^{36}Ar, ^{74}Ge is interfered by ^{36}Ar^{38}Ar, and ^{76}Ge is interfered by ^{36}Ar^{40}Ar. Other interferences are present at mass/charge ratio (m/e) 70 (e.g., ^{70}Zn) and 73. The precise measurement of Ge required minimization of the background contribution from Ar dimers at ^{74}Ge. Since the Ar dimers in the blank spectrum do not scale with increasing laser spot size and repetition rate, the largest spot size (150 μm) and a high repetition rate (50 Hz) were used to yield blank contributions on ^{74}Ge from ^{36}Ar^{38}Ar < 5%. At this high beam intensity, the variability of the blank contributed negligibly to the precision of the measurement of Ge and even less to blanks for other elements whose abundances are much larger than that of Ge. However, analytical artifacts associated with mass loading become a concern (56) that were ameliorated by using identical parameters for samples and standards. To examine the sensitivity of Ge to the mass loading effect with the current analytical protocols adopted, a set of five spot measurements were performed with increasing spot sizes (25, 50, 100, and 150 μm) and variable laser repetition rates (20 and 50 Hz) on USGS glass BHVO-2g. Each measurement was calibrated against National Institute of Standards and Technology (NIST) SRM 610 and analyzed under the identical spot size and repetition rate. Precision improves as laser spot size and repetition rate are increased, but no discernible effect of mass loading is present. Following (57), SRM 612 is avoided in this study in preference to SRM 610 that couples better with lasers.

In this study, Ge was measured at m/e 74. Isobaric interferences from doubly charged REE ions, particularly ^{148}Nd^{++} and ^{148}Sm^{++}, on ^{74}Ge were corrected by subtracting the calculated abundances of each isotope inferred from the doubly charged odd isotopes ^{145}Nd^{++} (m/e 72.5) and ^{149}Sm^{++} (m/e 74.5) monitored simultaneously. The magnitude of the corrections applied was 1% for ^{148}Sm^{++} and 2 to 3% for ^{148}Nd^{++} for all MORB samples, except those from the MCR where the corrections were 2% for ^{148}Sm^{++} and 4 to 5% for ^{148}Nd^{++}. The magnitude of the isobaric corrections on ^{74}Ge was similar for D-, N-, and E-MORBs. To examine whether the corrections were sufficient, the ^{148}Nd$^{++}/^{145}$Nd^{++} ratio was directly measured on a

Durango apatite crystal containing high REEs (Nd, 1500 ppm; Sm, 200 ppm) and negligible Ge. Application of this directly determined ratio systematically increased the measured Ge abundance of MORB glasses by only 0.3%, relatively verifying that the REE^{++} correction applied in this study was sufficient.

Elemental abundances were calculated from measured intensity ratios to ^{29}Si using relative sensitivity factors (RSFs) obtained from the USGS standards (BCR-2g, BHVO-2g, and BIR-1g), VG 2, and NIST SRM 610 (table S1). We noticed that the RSF of Sc obtained from BHVO-2g is systematically 10% higher than that obtained from BCR-2g and BIR-1g. In 17 LA-ICP-MS analyses compiled in the online GeoReM database, the Sc contents of BHVO-2g vary from 27 to 36 ppm, although only 6 of 46 analyses have Sc contents higher than 33 ppm (58) with the rest close to the 31 ppm value. When using the Sc abundance of 31 ppm (58), the RSFs of Sc obtained in the three USGS glasses are mutually consistent.

The composition of major elements and ScGe in the minerals, including olivine, clinopyroxene, orthopyroxene, and spinel, from seven San Carlos xenoliths were analyzed using the LA-ICP-MS operating in medium resolution and limited to elements from Na-Ge. For each mineral, we analyzed three to four grains per sample, and the averaged compositions are given in table S2. Bulk major element compositions determined by x-ray fluorescence (XRF) on fused whole-rock powders (59) are available for five of seven xenoliths analyzed in this study. The ratio of olivine to pyroxenes was calculated from CIPW norms to obtain mineral modes of these xenoliths from which bulk Ge abundances were calculated (table S2).

SUPPLEMENTARY MATERIALS

Supplementary material for this article is available at http://advances.sciencemag.org/cgi/content/full/6/26/eaba2923/DC1

REFERENCES AND NOTES

1. A. W. Hofmann, Chemical differentiation of the Earth: The relationship between mantle, continental crust, and oceanic crust. *Earth Planet. Sci. Lett.* **90**, 297–314 (1988).
2. V. J. M. Salters, A. Stracke, Composition of the depleted mantle. *Geochem. Geophys. Geosyst.* **5**, Q05B07 (2004).
3. A. Gale, C. A. Dalton, C. H. Langmuir, Y. Su, J.-G. Schilling, The mean composition of ocean ridge basalts. *Geochem. Geophys. Geosyst.* **14**, 489–518 (2013).
4. J. G. Schilling, Iceland mantle plume: Geochemical study of Reykjanes ridge. *Nature* **242**, 5400 (1973).
5. Y. Niu, K. D. Collerson, R. Batiza, I. Wendt, Origin of enriched-type mid-ocean ridge basalt at ridges far from mantle plumes: The East Pacific Rise at 11°20′N. *J. Geophys. Res. Solid Earth* **104**, 7067–7087 (1999).
6. M. M. Hirschmann, E. M. Stolper, A possible role for garnet pyroxenite in the origin of the "garnet signature" in MORB. *Contrib. Mineral. Petrol.* **124**, 185–208 (1996).
7. C. L. Waters, K. W. W. Sims, M. R. Perfit, J. Blichert-Toft, J. Blusztajn, Perspective on the genesis of E-MORB from chemical and isotopic heterogeneity at 9–10°N east pacific rise. *J. Petrol.* **52**, 565–602 (2011).
8. A. Brunelli, A. Cipriani, E. Bonatti, Thermal effects of pyroxenites on mantle melting below mid-ocean ridges. *Nat. Geosci.* **11**, 520–525 (2018).
9. A. V. Sobolev, A. W. Hofmann, D. V. Kuzmin, G. M. Yaxley, N. T. Arndt, S.-L. Chung, L. V. Danyushevsky, T. Elliott, F. A. Frey, M. O. Garcia, A. A. Gurenko, V. S. Kamenetsky, A. C. Kerr, N. A. Krivolutskaya, V. V. Matvienkov, I. K. Nikogosian, A. Rocholl, I. A. Sigurdsson, N. M. Sushchevskaya, M. Teklay, The amount of recycled crust in sources of mantle-derived melts. *Science* **316**, 412–417 (2007).
10. M. Pertermann, M. M. Hirschmann, Anhydrous partial melting experiments on MORB-like eclogite: Phase relations, phase compositions and mineral-melt partitioning of major elements at 2-3 GPa. *J. Petrol.* **44**, 2173–2201 (2003).
11. C. Hémond, A. W. Hofmann, I. Vlastélic, F. Nauret, Origin of MORB enrichment and relative trace element compatibilities along the Mid-Atlantic Ridge between 10° and 24°N. *Geochem. Geophys. Geosyst.* **7**, Q12010 (2006).
12. M. Ulrich, C. Hémond, P. Nonnotte, K. P. Jochum, OIB/seamount recycling as a possible process for E-MORB genesis. *Geochem. Geophys. Geosyst.* **13**, Q0AC19 (2012).
13. K. E. Donnelly, S. L. Goldstein, C. H. Langmuir, M. Spiegelman, Origin of enriched ocean ridge basalts and implications for mantle dynamics. *Earth Planet. Sci. Lett.* **226**, 347–366 (2004).
14. Y. Niu, M. Regelous, I. J. Wendt, R. Batiza, M. J. O'Hara, Geochemistry of near-EPR seamounts: Importance of source vs. process and the origin of enriched mantle component. *Earth Planet. Sci. Lett.* **199**, 327–345 (2002).
15. F. A. Davis, M. Humayun, M. M. Hirschmann, R. S. Cooper, Experimentally determined mineral/melt partitioning of first-row transition elements (FRTE) during partial melting of peridotite at 3 GPa. *Geochim. Cosmochim. Acta* **104**, 232–260 (2013).
16. D. He, C. A. Lee, X. Yu, M. Farner, Ge/Si Partitioning in Igneous systems: Constraints from laser ablation ICP-MS measurements on natural samples. *Geochem. Geophys. Geosyst.* **20**, 4472–4486 (2019).
17. S. Yang, M. Humayun, V. J. M. Salters, Elemental systematics in MORB glasses from the Mid-Atlantic ridge. *Geochem. Geophys. Geosystems.* **19**, 4236–4259 (2018).
18. J. Gill, P. Michael, J. Woodcock, B. Dreyer, F. Ramos, D. Clague, J. Kela, S. Scott, K. Konrad, D. Stakes, Spatial and temporal scale of mantle enrichment at the Endeavour segment, Juan de Fuca Ridge. *J. Petrol.* **57**, 863–896 (2016).
19. W. G. Melson, T. O'Hearn, E. Jarosewich, A data brief on the Smithsonian Abyssal Volcanic Glass Data File. *Geochem. Geophys. Geosyst.* **3**, 1–11 (2002).
20. F. E. Jenner, H. St. C. O'Neill, Analysis of 60 elements in 616 ocean floor basaltic glasses. *Geochem. Geophys. Geosyst.* **13**, Q02005 (2012).
21. V. Le Roux, R. Dasgupta, C.-T. A. Lee, Recommended mineral-melt partition coefficients for FRTEs (Cu), Ga, and Ge during mantle melting. *Am. Mineral.* **100**, 2533–2544 (2015).
22. S. J. G. Galer, R. K. O'Nions, Chemical and isotopic studies of ultramafic inclusions from the San Carlos Volcanic Field, Arizona: A bearing on their petrogenesis. *J. Petrol.* **30**, 1033–1064 (1989).
23. A. Stracke, B. Bourdon, The importance of melt extraction for tracing mantle heterogeneity. *Geochim. Cosmochim. Acta* **73**, 218–238 (2009).
24. H. Cheng, H. Zhou, Q. Yang, L. Zhang, F. Ji, H. Dick, Jurassic zircons from the Southwest Indian Ridge. *Sci. Rep.* **6**, 26260 (2016).
25. S. Mallick, H. J. B. Dick, A. Sachi-Kocher, V. J. M. Salters, Isotope and trace element insights into heterogeneity of subridge mantle. *Geochem. Geophys. Geosyst.* **15**, 2438–2453 (2014).
26. S. Lambart, D. Laporte, P. Schiano, Markers of the pyroxenite contribution in the major-element compositions of oceanic basalts: Review of the experimental constraints. *Lithos* **160–161**, 14–36 (2013).
27. M. Tang, C.-T. A. Lee, K. Chen, M. Erdman, G. Costin, H. Jiang, Nb/Ta systematics in arc magma differentiation and the role of arclogites in continent formation. *Nat. Commun.* **10**, 235 (2019).
28. T. J. Falloon, D. H. Green, L. V. Danyushevsky, A. W. McNeill, The composition of near-solidus partial melts of fertile peridotite at 1 and 1.5 GPa: Implications for the petrogenesis of MORB. *J. Petrol.* **49**, 591–613 (2008).
29. F. A. Davis, M. M. Hirschmann, M. Humayun, The composition of the incipient partial melt of garnet peridotite at 3 GPa and the origin of OIB. *Earth Planet. Sci. Lett.* **308**, 380–390 (2011).
30. M. J. Walter, Melting of garnet peridotite and the origin of komatiite and depleted lithosphere. *J. Petrol.* **39**, 29–60 (1998).
31. W. F. McDonough, S.-S. Sun, The composition of the Earth. *Chem. Geol.* **120**, 223–253 (1995).
32. R. L. Rudnick, S. Gao, Composition of the continental crust. *Treatise Geochem.* **3**, 1–64 (2003).
33. M. S. Drummond, M. J. Defant, A model for Trondhjemite-Tonalite-Dacite Genesis and crustal growth via slab melting: Archean to modern comparisons. *J. Geophys. Res.* **95**, 21503–21521 (1990).
34. C. J. Allègre, D. L. Turcotte, Implications of a two-component marble-cake mantle. *Nature* **323**, 123–127 (1986).
35. A. Zindler, H. Staudigel, R. Batiza, Isotope and trace element geochemistry of young Pacific seamounts: implications for the scale of upper mantle heterogeneity. *Earth Planet. Sci. Lett.* **70**, 175–195 (1984).
36. S. Huang, M. Humayun, F. A. Frey, Iron/manganese ratio and manganese content in shield lavas from Ko'olau Volcano, Hawai'i. *Geochim. Cosmochim. Acta* **71**, 4557–4569 (2007).
37. B. Peucker-Ehrenbrink, A. W. Hofmann, S. R. Hart, Hydrothermal lead transfer from mantle to continental crust: the role of metalliferous sediments. *Earth Planet. Sci. Lett.* **125**, 129–142 (1994).
38. R. Kessel, M. W. Schmidt, P. Ulmer, T. Pettke, Trace element signature of subduction-zone fluids, melts and supercritical liquids at 120–180 km depth. *Nature* **437**, 724–727 (2005).
39. S. G. Nielsen, T. J. Horner, H. V. Pryer, J. Blusztajn, Y. Shu, M. D. Kurz, V. Le Roux, Barium isotope evidence for pervasive sediment recycling in the upper mantle. *Sci. Adv.* **4**, eaas8675 (2018).

40. T. Plank, C. H. Langmuir, The chemical composition of subducting sediment and its consequences for the crust and mantle. *Chem. Geol.* **145**, 325–394 (1998).

41. T. Kogiso, M. M. Hirschmann, M. Pertermann, High-pressure partial melting of mafic lithologies in the mantle. *J. Petrol.* **45**, 2407–2422 (2004).

42. S. Lambart, M. B. Baker, E. M. Stolper, The role of pyroxenite in basalt genesis: Melt-PX, a melting parameterization for mantle pyroxenites between 0.9 and 5 GPa. *J. Geophys. Res. Solid Earth* **121**, 5708–5735 (2016).

43. J. Korenaga, Initiation and evolution of plate tectonics on Earth: Theories and observations. *Annu. Rev. Earth Planet. Sci.* **41**, 117–151 (2013).

44. M. Tang, K. Chen, R. L. Rudnick, Archean upper crust transition from mafic to felsic marks the onset of plate tectonics. *Science* **351**, 372–375 (2016).

45. R. J. Stern, Evidence from ophiolites, blueschists, and ultrahigh-pressure metamorphic terranes that the modern episode of subduction tectonics began in Neoproterozoic time. *Geology* **33**, 557–560 (2005).

46. V. J. M. Salters, S. Mallick, S. R. Hart, C. E. Langmuir, A. Stracke, Domains of depleted mantle: New evidence from hafnium and neodymium isotopes. *Geochem. Geophys. Geosyst.* **12**, Q08001 (2011).

47. A. Stracke, F. Genske, J. Berndt, J. M. Koornneef, Ubiquitous ultra-depleted domains in Earth's mantle. *Nat. Geosci.* **12**, 851–855 (2019).

48. A. Sanfilippo, V. Salters, R. Tribuzio, A. Zanetti, Role of ancient, ultra-depleted mantle in Mid-Ocean-Ridge magmatism. *Earth Planet. Sci. Lett.* **511**, 89–98 (2019).

49. C. Hawkesworth, P. A. Cawood, B. Dhuime, Rates of generation and growth of the continental crust. *Geosci. Front.* **10**, 165–173 (2019).

50. O. Jagoutz, O. Müntener, M. W. Schmidt, J.-P. Burg, The roles of flux- and decompression melting and their respective fractionation lines for continental crust formation: Evidence from the Kohistan arc. *Earth Planet. Sci. Lett.* **303**, 25–36 (2011).

51. C. H. Langmuir, J. F. Bender, R. Batiza, Petrological and tectonic segmentation of the East Pacific Rise, 5°30′–14°30′ N. *Nature* **322**, 422–429 (1986).

52. H. Zhou, H. J. B. Dick, Thin crust as evidence for depleted mantle supporting the Marion Rise. *Nature* **494**, 195–200 (2013).

53. M. Humayun, F. A. Davis, M. M. Hirschmann, Major element analysis of natural silicates by laser ablation ICP-MS. *J. Anal. At. Spectrom.* **25**, 998–1005 (2010).

54. M. Humayun, Chondrule cooling rates inferred from diffusive profiles in metal lumps from the Acfer 097 CR2 chondrite. *Meteorit. Planet. Sci.* **47**, 1191–1208 (2012).

55. S. Yang, M. Humayun, K. Righter, G. Jefferson, D. Fields, A. J. Irving, Siderophile and chalcophile element abundances in shergottites: Implications for Martian core formation. *Meteorit. Planet. Sci.* **50**, 691–714 (2015).

56. F. E. Jenner, H. St. C. O'Neill, Major and trace analysis of basaltic glasses by laser-ablation ICP-MS. *Geochem. Geophys. Geosyst.* **13**, Q03003 (2012).

57. M. Gaboardi, M. Humayun, Elemental fractionation during LA-ICP-MS analysis of silicate glasses: implications for matrix-independent standardization. *J. Anal. At. Spectrom.* **24**, 1188 (2009).

58. K. P. Jochum, M. Willbold, I. Raczek, B. Stoll, K. Herwig, Chemical characterisation of the USGS reference glasses GSA-1G, GSC-1G, GSD-1G, GSE-1G, BCR-2G, BHVO-2G and BIR-1G Using EPMA, ID-TIMS, ID-ICP-MS and LA-ICP-MS. *Geostand. Geoanalytical Res.* **29**, 285–302 (2005).

59. A. D. Brandon, D. W. Graham, T. Waight, B. Gautason, [186]Os and [187]Os enrichments and high-[3]He/[4]He sources in the Earth's mantle: Evidence from Icelandic picrites. *Geochim. Cosmochim. Acta* **71**, 4570–4591 (2007).

60. C. Münker, J. A. Pfänder, S. Weyer, A. Büchl, T. Kleine, K. Mezger, Evolution of planetary cores and the Earth-Moon system from Nb/Ta systematics. *Science* **301**, 84–87 (2003).

61. D. A. Clague, B. M. Dreyer, J. B. Paduan, J. F. Martin, D. W. Caress, J. B. Gill, D. S. Kelley, H. Thomas, R. A. Portner, J. R. Delaney, T. P. Guilderson, M. L. McGann, Eruptive and tectonic history of the Endeavour Segment, Juan de Fuca Ridge, based on AUV mapping data and lava flow ages. *Geochem. Geophys. Geosystems.* **15**, 3364–3391 (2014).

62. R. Arevalo Jr., W. F. McDonough, P. M. Piccoli, In situ determination of First-Row transition metal, Ga and Ge abundances in geological materials via medium-resolution LA-ICP-MS. *Geostand. Geoanalytical Res.* **35**, 253–273 (2011).

63. K. P. Jochum, B. Stoll, K. Herwig, M. Willbold, A. W. Hofmann, M. Amini, S. Aarburg, W. Abouchami, E. Hellebrand, B. Mocek, I. Raczek, A. Stracke, O. Alard, C. Bouman, S. Becker, M. Dücking, H. Brätz, R. Klemd, D. de Bruin, D. Canil, D. Cornell, C.-J. de Hoog, C. Dalpé, L. Danyushevsky, A. Eisenhauer, Y. Gao, J. E. Snow, N. Groschopf, D. Günther, C. Latkoczy, M. Guillong, E. H. Hauri, H. E. Höfer, Y. Lahaye, K. Horz, D. E. Jacob, S. A. Kasemann, A. J. R. Kent, T. Ludwig, T. Zack, P. R. D. Mason, A. Meixner, M. Rosner, K. Misawa, B. P. Nash, J. Pfänder, W. R. Premo, W. D. Sun, M. Tiepolo, R. Vannucci, T. Vennemann, D. Wayne, J. D. Woodhead, MPI-DING reference glasses for in situ microanalysis: New reference values for element concentrations and isotope ratios. *Geochem. Geophys. Geosyst.* **7**, Q02008 (2006).

64. A. Makishima, E. Nakamura, Determination of Ge, As, Se and Te in silicate samples using isotope dilution-internal standardisation octopole reaction cell ICP-QMS by normal sample nebulisation. *Geostand. Geoanalytical Res.* **33**, 369–384 (2009).

65. K. P. Jochum, B. Stoll, U. Weis, D. E. Jacob, R. Mertz-Kraus, M. O. Andreae, Non-matrix-matched calibration for the multi-element analysis of geological and environmental samples using 200 nm femtosecond LA-ICP-MS: A comparison with nanosecond lasers. *Geostand. Geoanalytical Res.* **38**, 265–292 (2014).

66. F. E. Jenner, R. J. Arculus, J. A. Mavrogenes, N. J. Dyriw, O. Nebel, E. H. Hauri, Chalcophile element systematics in volcanic glasses from the northwestern Lau Basin. *Geochem. Geophys. Geosyst.* **14**, Q06014 (2012).

67. J. Hertogen, M.-J. Janssens, H. Palme, Trace elements in ocean ridge basalt glasses: implications for fractionations during mantle evolution and petrogenesis. *Geochim. Cosmochim. Acta* **44**, 2125–2143 (1980).

68. R. M. de Argollo, J. G. Schilling, Ge/Si and Ga/Al variations along the Reykjanes Ridge and Iceland. *Nature* **276**, 24–28 (1978).

69. K. A. Kelley, R. Kingsley, J.-G. Schilling, Composition of plume-influenced mid-ocean ridge lavas and glasses from the Mid-Atlantic Ridge, East Pacific Rise, Galápagos Spreading Center, and Gulf of Aden. *Geochem. Geophys. Geosyst.* **14**, 223–242 (2013).

70. G. M. Yaxley, D. H. Green, Reactions between eclogite and peridotite: mantle refertilisation by subduction of oceanic crust. *Schweiz Miner. Petrogr.* **78**, 243–255 (1998).

71. M. Pertermann, M. M. Hirschmann, K. Hametner, D. Günther, M. W. Schmidt, Experimental determination of trace element partitioning between garnet and silica-rich liquid during anhydrous partial melting of MORB-like eclogite. *Geochem. Geophys. Geosyst.* **5**, Q05A01 (2004).

72. M. Pertermann, M. M. Hirschmann, Partial melting experiments on a MORB-like pyroxenite between 2 and 3 GPa: Constraints on the presence of pyroxenite in basalt source regions from solidus location and melting rate. *J. Geophys. Res. Solid Earth* **108**, 2125 (2003).

73. V. J. Salters, J. Longhi, Trace element partitioning during the initial stages of melting beneath mid-ocean ridges. *Earth Planet. Sci. Lett.* **166**, 15–30 (1999).

74. P. McDade, J. D. Blundy, B. J. Wood, Trace element partitioning on the Tinaquillo Lherzolite solidus at 1.5GPa. *Phys. Earth Planet. Inter.* **139**, 129–147 (2003).

75. R. K. Workman, S. R. Hart, Major and trace element composition of the depleted MORB mantle (DMM). *Earth Planet. Sci. Lett.* **231**, 53–72 (2005).

76. J. A. Pfänder, C. Münker, A. Stracke, K. Mezger, Nb/Ta and Zr/Hf in ocean island basalts — Implications for crust–mantle differentiation and the fate of Niobium. *Earth Planet. Sci. Lett.* **254**, 158–172 (2007).

77. V. J. M. Salters, The generation of mid-ocean ridge basalts from the Hf and Nd isotope perspective. *Earth Planet. Sci. Lett.* **141**, 109–123 (1996).

78. A. V. Sobolev, A. W. Hofmann, S. V. Sobolev, I. K. Nikogosian, An olivine-free mantle source of Hawaiian shield basalts. *Nature* **434**, 590–597 (2005).

79. M. S. Ghiorso, M. M. Hirschmann, P. W. Reiners, V. C. Kress III, The pMELTS: A revision of MELTS for improved calculation of phase relations and major element partitioning related to partial melting of the mantle to 3 GPa. *Geochem. Geophys. Geosyst.* **3**, 1–35 (2002).

80. C. H. Langmuir, E. M. Klein, T. Plank, Petrological systematics of mid-ocean ridge basalts: Constraints on melt generation beneath ocean ridges, in *Mantle Flow Melt Generation at Mid-Ocean Ridges*, J. P. Morgan, D. K. Blackman, J. M. Sinton, Eds. (AGU Monograph, Washington, DC, 1993), vol. **71**, pp. 183–280.

81. A. V. Sobolev, E. V. Asafov, A. A. Gurenko, N. T. Arndt, V. G. Batanova, M. V. Portnyagin, D. Garbe-Schönberg, A. H. Wilson, G. R. Byerly, Deep hydrous mantle reservoir provides evidence for crustal recycling before 3.3 billion years ago. *Nature* **571**, 555–559 (2019).

82. W. B. Hamilton, Earth's first two billion years-The era of internally mobile crust, in *4-D Framework of Continental Crust: Geological Society of America Memoir* (2007), vol. **200**, pp. 233–296.

83. D. Andrault, G. Pesce, M. A. Bouhifd, N. Bolfan-Casanova, J.-M. Hénot, M. Mezouar, Melting of subducted basalt at the core-mantle boundary. *Science* **344**, 892–895 (2014).

84. E. Anders, N. Grevesse, Abundances of the elements: Meteoritic and solar. *Geochim. Cosmochim. Acta* **53**, 197–214 (1989).